Nanoscale

Fabrication of Pyramidal (111) $MAPbBr_3$ Film with Low Surface Defect Density Using Homogeneous Quantum-Dot Seeds

Journal:	*Nanoscale*
Manuscript ID	NR-COM-11-2019-010070
Article Type:	Communication
Date Submitted by the Author:	18-Nov-2019
Complete List of Authors:	Jeong, Hyeon Jun; Sungkyunkwan University - Suwon Campus, Department of Energy Science Bang, Seungho; Sungkyunkwan University - Suwon Campus, Department of Energy Science Park, Dae Young; Sungkyunkwan University, Department of Energy Science; Center for Integrated Nanostructure Physics (CINAP) Jeon, Hobeom; Sungkyunkwan University - Suwon Campus, Department of Energy Science Gon, Namkoon; Old Dominion University, Electrical and Computer Engieering Jeong, Mun Seok; Sungkyunkwan University, Department of Energy Science

SCHOLARONE™
Manuscripts

Please do not adjust margins

COMMUNICATION

Fabrication of Pyramidal (111) $MAPbBr_3$ Film with Low Surface Defect Density Using Homogeneous Quantum-Dot Seeds

Received 00th January 20xx,
Accepted 00th January 20xx

DOI: 10.1039/x0xx00000x

Hyeon Jun Jeong,[a] Seungho Bang,[a] Dae Young Park,[a] Hobeom Jeon,[a] Gon Namkoong*[b] and Mun Seok Jeong *[a]

Nucleation and seeding of organometal halide perovskite (OHP) films have been extensively investigated for forming high-density, large-crystalline, and low-defect films. In this study, $CH_3NH_3PbBr_3$ ($MAPbBr_3$) films with a low defect density are synthesized via a molecular exchange mechanism using $MAPbBr_3$ quantum dots as seeds. The synthesized films exhibit a pyramidal morphology with a (111) crystal plane. The distribution of the (111) plane is controlled by adjusting the seed concentration. The pyramidal $MAPbBr_3$ films exhibit improved photoluminescence intensity and uniformity compared with films produced using seedless toluene. When the seeds are employed, the surface trap density is reduced by a factor of 3.5, suppressing the photocurrent hysteresis and nonsaturated response of photodetectors. Additionally, the films formed using the seeds have improved stability owing to the chain decomposition reaction induced by electron beam heating.

Introduction

Organometal halide perovskite (OHP) materials have innate photo-electric properties[1,2] and have revolutionized many aplications, including solar cells,[3-5] photodetectors,[6] transistors,[7] memory devices,[8] and light-emitting diodes.[9,10] Widely used low-cost production methods for OHPs include vapor deposition,[11] the inkjet printing technique,[12] anti-solvent crystallization,[9,13] and two-step deposition.[3,14] These methods mainly focus on regulating the morphology, grain size of the crystal and the coverage of the film. However, OHP films produced via the aforementioned methods typically contain random crystal orientations, resulting in poor charge transport and a high trap density.[9,10,13,14] Thus, the uncontrolled polarity of the atomic arrangement along the crystal orientation may limit the performance of the optoelectronic perovskite device by inducing different band structures between the planes.[15,16]

The crystal orientation and trap density are significantly dependent on the nucleation stage of the crystal growth.[17-19] Thus, interest in research for controlling the orientation has increased. For instance, Yang *et al*. introduced an intramolecular exchange mechanism by using a PbI_2-dimethyl sulfoxide(DMSO) or $PbI_2(PbBr_2)$-DMSO seed layer to produce (111)-oriented OHP films.[20] Remarkably, the controlled orientation of the film led to a perovskite solar cell with suppressed hysteresis, high reliability, and a power conversion efficiency (PCE) of 22.6%.[20] Furthermore, Zhao *et al*. introduced seeds (colloidal perovskite) embedded in the PbI_2 layer to support crystallization.[21] In this method, a (001)-oriented $FAPbI_3$ film with a low trap density was formed using two-step sequential deposition, resulting in a stabilized PCE of 21.5%.[21] Additionally, Bi *et al*. synthesized highly oriented OHP films with high crystallinity, suppressed hysteresis, and a large grain size by utilizing poly(methyl methacrylate) for polymer-templated nucleation.[22] Although these seed-based nucleation methods successfully produced highly oriented crystal planes, the crystal orientation of the film has not yet been fully controlled. Furthermore, the OHP films contain many defects in the bulk and on the surface owing to vacancy and interstitial defects that typically have a low defect formation energy.[23] In particular, many surface or interfacial trap states have detrimental hysteresis effects for optical devices.[24,25] For instance, Kim *et al*. fabricated [-111]-axial films and achieved a low trap density ($\sim 4 \times 10^{14}\ cm^{-3}$) by using a topotactic reaction involving Cl-containing intermediates.[26] Cho *et al*. fabricated OHP films oriented with (112) and (200) planes using a thermal-gradient-assisted directional crystallization method and achieved a low trap density of $\sim 7.9 \times 10^{13}\ cm^{-3}$.[27] Even though OHP films with remarkably low trap densities were obtained using these methods, the hysteresis of the solar cells and photodetectors was observed, possibly owing to the presence of considerable surface or interfacial trap states.

In the present study, to address these issues, a new structural $MAPbBr_3$ fabrication method using $MAPbBr_3$ quantum dots (QDs) as nano-seeds was investigated. The preferential growth of the $MAPbBr_3$ films toward the (111) plane was achieved via two molecular-exchange processes of the nano-seeds. The growth planes [(100) and (111) planes] of the $MAPbBr_3$ films were strongly dependent on the $MAPbBr_3$

[a] *Department of Energy Science, Sungkyunkwan University, Suwon 16419, Republic of Korea*
[b] *Department of Electrical and Computer Engineering, Old Dominion University, Applied Research Centre, 12050 Jefferson Avenue, Newport News, USA*
† Footnotes relating to the title and/or authors should appear here.
Electronic Supplementary Information (ESI) available: Materials and Methods, Figure S1-S9, Table S1,S2. See DOI: 10.1039/x0xx00000x

This journal is © The Royal Society of Chemistry 20xx

Please do not adjust margins

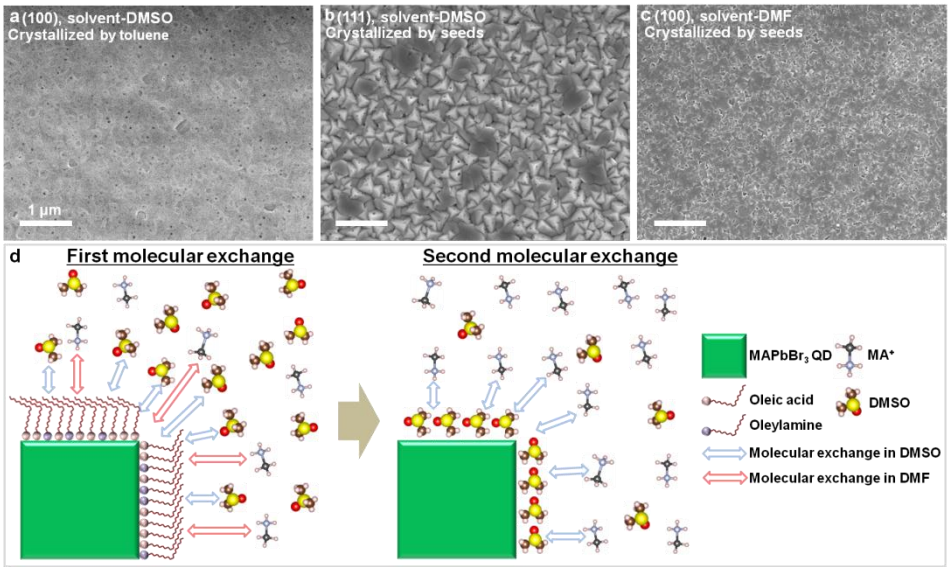

Figure 1. SEM images of films produced under different conditions. The solvent of the perovskite solution was a, b) DMSO or c) DMF. The film was crystallized by a) toluene or b, c) seeds. d) Schematic of the growth mechanism induced by seeds. When DMF was used, the first molecular exchange (pink arrows) occurred. When DMSO was used, the first and second molecular exchanges (sky blue arrows) occurred.

nano-seed concentration. Confocal scanning photoluminescence microscopy (CSPLM) revealed that a film grown in the (111) plane with nano-seeds exhibited a photoluminescence (PL) intensity approximately seven times higher than that of a film grown in the (100) plane without nano-seeds. In addition, [111] oriented films with nano-seeds exhibited a more uniform PL image. Furthermore, optoelectronic measurements revealed that the photocurrent hysteresis and the non-saturated response of photodetectors were suppressed in the $MAPbBr_3$ film fabricated with nano-seeds.

Results and discussion

The fabrication process of $MAPbBr_3$ films by using the nano-seed approach is similar to the anti-solvent crystallization method.[9,13] In our experiment, we dispersed $MAPbBr_3$ quantum dots as nano-seeds in an anti-solvent for film crystallization (Figure S1). To investigate the crystallization mechanism induced by the nano-seeds, the $MAPbBr_3$ precursor solution was prepared using DMSO and dimethylformamide (DMF) as solvents. Once the seed layer was dropped onto the substrate, the films were spin-coated at 4000 rpm for 40s and 5s for DMSO and DMF, respectively, to achieve a uniform coating. The seed-induced crystallization occurred instantaneously, without intermediate states. Figures 1a–c present scanning electron microscopy (SEM) images showing the surface morphologies of seed layers fabricated with different solvents and seed conditions. When crystallization was performed using DMSO as a solvent and toluene as an antisolvent (Figure 1a), the film had no distinct shape, but the (100) plane dominated in the X-ray diffraction (XRD) pattern (Figure S2a). However, there was a parasitic peak around the (100) plane in the log-scale XRD pattern (Figure S2c). The presence of this parasitic peak indicates that there was another phase in the film formed by toluene.[28, 29] Crystallization using seeds (Figure 1b) with DMSO as solvent showed triangular crystals and (111) plane without parasitic peaks clearly dominant in the XRD pattern (Figure S2b, S2c). Additionally, as the volume ratio of the DMF solvent increased, the (100) plane became dominant, as shown in the XRD pattern (Figure S2b), and (100) cubic-shaped crystals were observed in the SEM image (Figure 1c). Through the experiments with three different conditions, we can estimate the growth mechanism by the seed, as illustrated in Figure 1d. Figure 1d shows a schematic of the two-step molecular exchange induced by $MAPbBr_3$ seeds for different solvents. When the seed is introduced, in the first molecular exchange the DMSO acting as a ligand is distributed at a higher concentration than the other molecules around the seed. Thus, the ligand surrounding the seed preferentially undergoes molecular exchange with DMSO. In the second exchange of molecules, DMSO is evaporated with toluene during spin coating and eventually the concentration of DMSO is reduced resulting in additional molecular exchange with MA^+. In this process, (111) surface growth occurs preferentially owing to the molecular exchange of the seeds and the triangular pyramid molecular structure of DMSO. When DMF is used as a solvent, however, DMF does not act as a ligand. In this case, molecular exchange occurs immediately between the ligand and MA^+ in the first molecular exchange step, leading to crystal growth. Precursor solutions using DMF are readily crystallized by evaporation of DMF during spin-coating times of 5 seconds, making it difficult to achieve full coverage (Figure S2d).

The $MAPbBr_3$ QDs used as the seeds were produced via a conventional ligand-assisted reprecipitation method.[30] The seed concentration was defined by the amount of the seed precursor in the toluene. Figures S3a–c show the absorption spectra of the seeds with respect to the seed concentration and aggregation time. As the seed concentration increased

 This journal is © The Royal Society of Chemistry 20xx

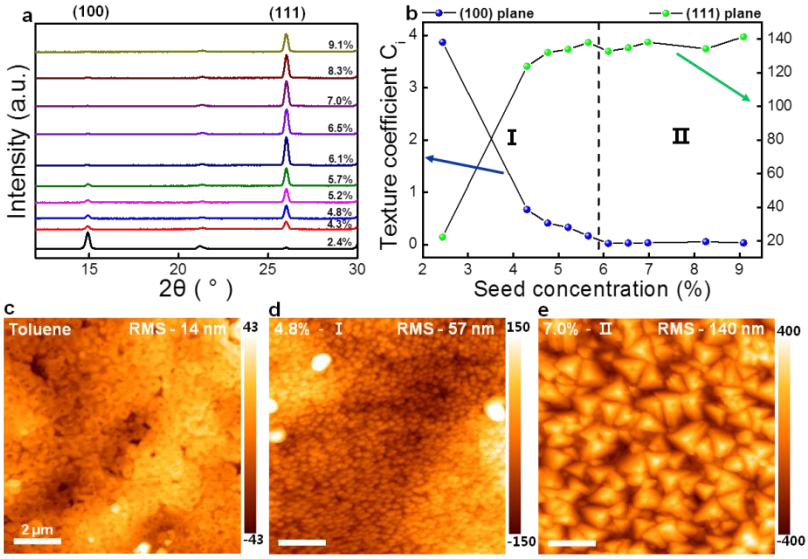

Figure 2. a) XRD patterns of $MAPbBr_3$ films fabricated with seed concentrations ranging from 2.4% to 9.1%. b) Calculated texture coefficient values for the (100) and (111) planes of the aforementioned films. AFM images of $MAPbBr_3$ films formed with c) toluene and seed concentrations of d) 4.8% and e) 7.0%.

from 2.0% to 9.1%, the exciton peaks were red-shifted owing to the aggregation of seeds.[31] The exciton peak positions for seed concentrations of 9.1% and 3.8% were 2.65 and 2.73 eV, respectively, as shown in the Figure S3a. The seeds gradually aggregated over time from 30 min to 4 h. For instance, the exciton peak positions for a seed concentration of 9.1% were red-shifted to 2.65, 2.60 and 2. 56 eV after 30 min, 2 h, and 4 h, respectively. Low seed concentrations of 2.0%–5.7% resulted in slow seed aggregation. In contrast, high seed concentrations of 7.4%–9.1%, resulted in rapid aggregation and relatively large aggregates, yielding a drastic reduction in the absorbance over time. These results indicate that as the seed density of toluene gradually decreases over time, the seed size increases through aggregation. Therefore, the aggregation time was fixed at 90 min to tightly control the seed size and density. Transmission electron microscopy (TEM) was measured to more directly observe the change in seed size with the concentration of MAPbBr3 seed. Figures S3d-f show TEM images of 4.8%, 7.0% and 12.0% $MAPbBr_3$ seeds. The seed size varied due to its rapid aggregation characteristics. The average sizes of 4.8%, 7.0% and 12.0% MAPbBr3 seeds were about 3.2nm, 4.5nm and 5.2nm, respectively.

The structural properties of films crystallized with precisely controlled seed concentrations were analyzed via XRD patterns. Figure 2a presents the XRD patterns of films formed with seed concentrations ranging from 2.4% to 9.1% on an indium tin oxide substrate. Diffraction peaks associated with $MAPbBr_3$ are observed at 14.92° and 26.02°, which are assigned to the (100) and (111) planes of $MAPbBr_3$, respectively. As the seed concentration increased, the distribution of the (100) plane decreased, but the (111) plane started to dominate. This is because as the concentration of the seeds increased, the density and size of the seeds in the toluene increased. As a consequence, the specific gravity of the (111) plane was facilitated by two-step molecular exchanges, illustrated in Figure 1d. The texture coefficients were calculated to quantify the preferred orientation of the crystals with an increase in the concentration of the $MAPbBr_3$ seeds.[32,33] The texture coefficient values can indicate the principal plane of the film compared to the peak intensity of the random powder diffraction. To derive this, the relative intensity of each plane in the diffraction pattern of a completely random powder is required. Therefore, the diffraction patterns of the powder of the perovskite single crystals were measured, as shown in Figure S4.[34] The texture-coefficient C_i was calculated using Equation (1).[32,33]

$$C_i = (I_i/I_{i0})/[(1/N)\sum_{i=1}^{N}(I_i/I_{i0})] \quad \ldots (1)$$

where I_i and I_{i0} represent the diffraction peak intensities of the film and random powder, respectively, and N represents the number of considered diffraction planes. The calculated values of the (100) and (111) planes based on the seed concentration are shown in the graph of Figure 2b. As the seed concentration increased, the texture coefficient values of the (100) plane approached zero. The texture-coefficient values of the (111) plane approached approximately 140. To examine the crystal orientation with respect to the seed concentration, the plot was divided into two sections according to the texture-coefficient value. As the seed concentration increased in section Ⅰ, the contribution of the (100) planes decreased sharply, and the growth of the (111) planes started to dominate. In section Ⅱ, the texture-coefficient value of the (111) plane saturated to approximately 140 and that of the (100) plane became approximately 0. In section Ⅰ, both the (100) and (111) planes coexisted. In section Ⅱ, the preferred growth direction was completely changed to the [111] direction. With a seed concentration of 7.0%, the texture coefficients of the (100) and (111) planes were 0.03 and 138.24, respectively, confirming a [111] directional $MAPbBr_3$

film growth. Thus, by utilizing the phenomenon of increasing seed density and size with increasing seed concentration, the preferred film orientation can be perfectly controlled from (100) plane to (111) plane.

To observe the morphological changes with the seeds, atomic force microscopy (AFM) images of the toluene crystallized film (seed concentration of zero), the section Ⅰ film (seed concentration of 4.8%), and section Ⅱ film (seed concentration of 7.0%) were acquired. Note that the calculated concentration of seeds for the 4.8% and 7.0% films after 90 mins of the aggregation time were 136 and 122 μM respectively (Figure S5).[35] Figure 2c shows a film crystallized by toluene without seeds, which exhibited dark spots. Figures 2d and e show films formed by the seeds with concentrations of 4.8% and 7.0%, respectively. The size of the crystals was approximately 270 and 1033 nm, respectively (crystal size was calculated using the random line profile).[36] As shown in Figures S3d-f, the seed size increased with high seed concentration, leading to a larger crystal size of the film. Additionally, the pyramidal shape dominated, which corresponds to (111) plane crystals with a clean surface.

The absorption spectra, CSPLM images and the time-resolved PL (TRPL) were measured to investigate the optical properties of the films formed by the seeds. Figure S6a shows the absorption spectra of the films formed with toluene and seed concentrations of 4.8% and 7.0%. As the seed concentration increased, the film became thicker and consequently the absorbance increased. Particularly, the thick $MAPbBr_3$ film by the seeds is likely to be caused by an increase in the total amount of MA^+, Pb^{+2} and Br^- ions in $MAPbBr_3$ seed precursors. We note the role of MA^+, Pb^{+2} and Br^- ions in the nucleation or crystal growth processes. When the seeds were injected into the quasi-film, we believe that the MA^+, Pb^{+2} and Br^- ions inside quasi-film did not participate in nucleation process. This is because additional nucleation reaction are not required for $MAPbBr_3$ crystal formation. Instead, the MA^+, Pb^{+2} and Br^- ions of the quasi-film contributed to increasing the size of $MAPbBr_3$ crystals through a two-step molecular exchange process on the seeds, illustrated in Figure 1d. Accordingly, an increase in absorbance (Figure S6a, b) is attributed to an increase in the thickness of the film by the seeds. The excitonic peaks of the films formed with toluene (without seeds), a seed concentration of 4.8%, and a seed concentration of 7.0% were 2.38, 2.37 and 2.36 eV, respectively. The films formed by the seeds exhibited red-shift compared with the films formed by toluene without seeds. To further analyze this phenomenon, CSPLM was performed. Figures 3a, c, e and Figures 3b, d, f present the integrated PL intensity images and peak-position images of the films formed with toluene and seed concentrations of 4.8% and 7.0%, respectively. As shown in Figures 3a, c, and e, the maximum integrated intensities of the films formed with seed concentrations of 4.8% and 7.0% were improved by factors of approximately 7.3 and 5.3, respectively, compared with that of the film formed by toluene. Additionally, in the histograms of the integrated intensity, the films formed with the seeds exhibited an improved distribution and uniformity in the high intensity (Figure S6c). As shown in

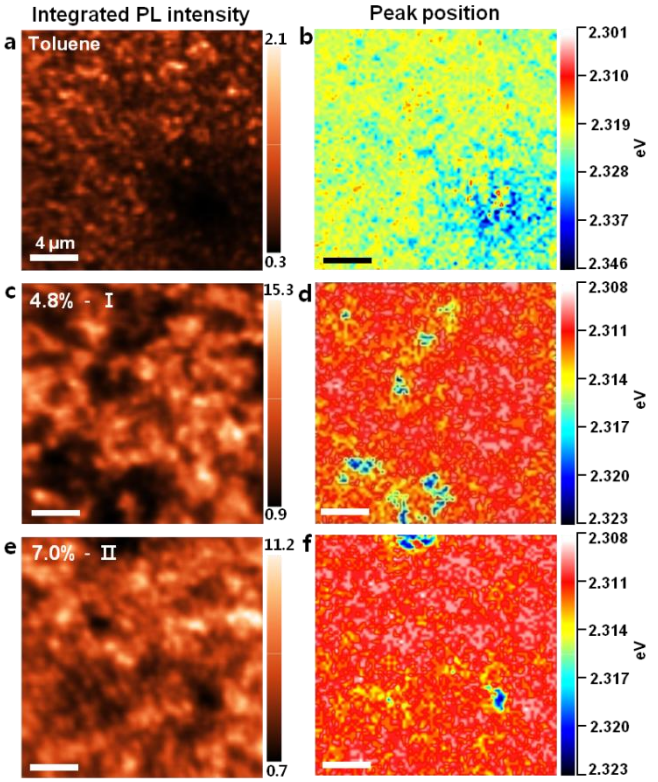

Figure 3. Integrated PL intensity image of $MAPbBr_3$ films formed with a) toluene and seed concentrations of c) 4.8% and e) 7.0%. Peak-position images of $MAPbBr_3$ films formed with b) toluene and seed concentrations of d) 4.8% and f) 7.0%. The integrated PL intensity image and peak-position image of each condition are in the same region.

Figures 3b, d and f, the peak energy of the films formed with toluene and the seeds were distributed with peaks at approximately 2.319 and 2.311 eV, respectively. This indicates that the band gap energy of the crystal with a (100) plane formed by toluene was higher than that of the crystal with a (111) plane formed by the seeds. In Figures 3d and f, the high-energy region (blue color) coincides with the low intensity region at the integrated PL intensity. This is consistent with the energy (2.319 eV) being mainly distributed in the film formed by toluene; thus, the (100) plane formed by the toluene remained in the film formed by the seeds. Furthermore, we measured the TRPL of the films formed with toluene and seed concentrations of 4.3% and 7.0%. The decay curves in Figure S6d were analyzed via bi-exponential decay fitting. The fitted values are presented in Table S1. The decay curves were divided into fast components τ_1 (toluene , 0.36 ns; 4.3%, 0.54 ns; 7.0%, 0.55 ns) and slow components τ_2 (toluene, 2.54 ns; 4.3%, 1.82 ns; 7.0%, 1.46 ns). The fast component was mainly attributed to the trap-assisted recombination caused by the non-stoichiometric trap sites such as the grain boundaries on the surface, whereas the slow component was attributed to the radiative recombination of the inner bulk.[9,10,15-17] With regard to the fast component, the lifetime of the film formed by toluene was shorter than that of the film formed by the seed. Additionally, as the seed concentration increased, the

This journal is © The Royal Society of Chemistry 20xx

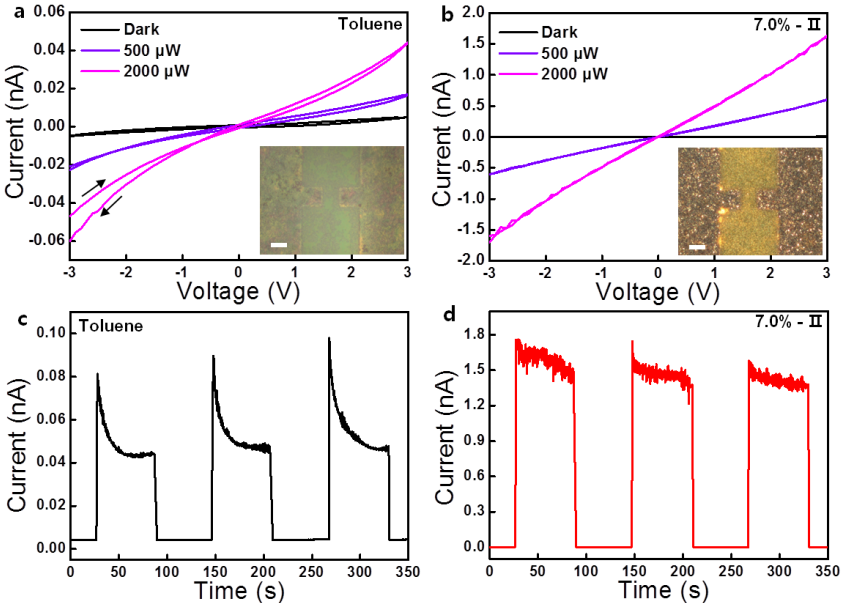

Figure 4. *I–V* characteristics of photodetectors using the films fabricated with a) toluene and b) a seed concentration of 7.0% in the dark, at 500 μW, and at 2000 μW. Inset figure is the top-view of each photodetectors. Scale bar is 15 μm. Time-dependent on/off photocurrents at 2000 μW for the films fabricated with c) toluene and d) a seed concentrations of 7.0% at 3 V.

fraction f_1 (toluene, 59%; 4.3% seed concentration, 38%; 7.0% seed concentration, 25%) decreased. This indicates that the specific gravity of the trap-assisted recombination decreased. Conversely, as the seed concentration increased, the f_2 value (toluene, 41%; 4.3% seed concentration, 62%; 7.0% seed concentration, 75%) corresponding to the slow component increased. Notably, the τ_2 was short despite the improved PL intensity, which can be associated to band strucutres of films.[9,10,15-17] Note that many reports[37-39] discuss a mix of direct and indirect band structures of OHPs due to the strain induced by the rotation of the organic cation. From XRD measurement, we found that the films with the (111) plane have much smaller lattice parameters than the films with (100) plane [Figure 2a, (111) plane – 2.71 Å and (100) plane – 5.84 Å]. This implies that the rotation of the organic cation MA^+ in the $MAPbBr_3$ film formed with the (111) plane is unlikely due to the small lattice parameter of the inorganic lattice. Therefore, the $MAPbBr_3$ film with the (111) plane has a direct band structure due to the reduced cation-induced strain, leading to a short carrier lifetime and red-shifted band gap of the $MAPbBr_3$ film with the (111) plane.[37-39] The average lifetime of the film formed by toluene was short because the fraction f_1 of the τ_1 value related to trap assisted recombination was large.

To investigate the effect of the seed (7.0%) on the trap density of the $MAPbBr_3$ film, the differential equation of the initial generated charge carrier density by the excitation power dependent PL was utilized.[40,41] The initial generated charge carrier density n(0) is defined by Equation (2):

$$n(0) = \sum_i N_T^i(0)\left(1 - \exp(-a_i \tau_0 I_{PL}/k)\right) + I_{PL}/k \quad \ldots (2)$$

where n_T^i represents the initial unfilled trap state density, a_i represents the product of the trap cross section and carrier velocity, τ_0 represents the PL lifetime, I_{PL} represents the integrated PL intensity, and k is a constant for a given sample. Figure S7 shows the initial generated charge carrier density with respect to the normalized PL intensity. This can be described by the surface and bulk trap density through fitting of the differential equation. The bulk trap density of the film formed by toluene was $n_T^b \approx 1.47 \times 10^{16}\ cm^{-3}$ and the surface trap density was $n_T^s \approx 8.35 \times 10^{17}\ cm^{-3}$. For the film formed with seeds, the bulk trap density was $n_T^b \approx 1.22 \times 10^{16}\ cm^{-3}$, and the surface trap density was $n_T^s \approx 2.36 \times 10^{17}\ cm^{-3}$. These trap-density values are similar to previously reported values.[40,41] The surface trap density of the film formed with seeds was approximately 3.5 times lower than that of the film formed by toluene. To investigate the effect of the significantly reduced surface trap density on the photocurrent hysteresis, the photocurrent was measured by fabricating an $MAPbBr_3$ film on a substrate with an Au electrode deposited on silicon dioxide.[24,25,42] It was measured at powers of 500 and 2000 μW using a 458-nm excitation laser. Figures 4a and b show the forward bias and reverse bias from −3 to 3 V for the films formed by toluene and with a seed concentration of 7.0%, respectively. The inset shows an optical microscope image of each $MAPbBr_3$ film on the substrate with an Au electrode. The active area was 20μm × 20μm. The film formed by toluene had photocurrents of 1.689×10^{-11} A at 3 V with 500 μW and 4.417×10^{-11} A at 3 V with 2000 μW. The film formed with the seed concentration of 7.0% had photocurrents of 5.989×10^{-10} A at 3 V with 500 μW and 1.638×10^{-9} A at 3 V with 2000 μW. The photocurrent of the film formed with the seed was improved by a factor of approximately 37 compared with that of the film formed by toluene under a power of 2000 μW. This is due to the smooth carrier migration provided by the (111) plane formed by the

seeds without parasitic peaks, as shown in Figure S2c. Additionally, the improvement is attributed to the enhanced uniformity and intensity, as shown in the CSPLM images of Figure 3. Furthermore, it might have been due to the increase in absorbance, which is attributed to the film-thickness increase shown in Figures S4a and b. This result indicates that the photocurrent hysteresis disappears by suppressing surface defects of the film formed by the seed. In this regard, Figures 4c and d show the time-dependent on/off photocurrent measured at 3 V with 2000 μW. The spike shaped peak is caused by non-saturated response. Most of the photo-generated carriers were located near the surface owing to the high absorption coefficient of the $MAPbBr_3$, i.e., approximately 10^5 at 458 nm.[43] The carriers trapped in the surface defects were excited by the bias and laser, which ultimately contributed to the photocurrent. Thereafter, the excited carriers were again trapped the surface traps, and leading to a non-saturated response.[44,45] As shown in Figure 4c, the ratio of the saturation current to the peak current was approximately 1:0.86, and it increased to 1:1.1 over time owing to the degradation caused by light irradiation.[46,47] As shown in Figure 4d, the film formed by the seeds had a low surface defect density; thus the ratio of the saturation current to the peak current was approximately 1:0.17. The suppressed photocurrent hysteresis and non-saturated response clearly indicate the reduction of the surface trap density. The surface trap density decreased for the following reason; 1) The injection of the completed $MAPbBr_3$ seed did not require the nucleation point of the $MAPbBr_3$ crystal to be formed on the heterogeneous substrate. The crystals to be formed by the seeds reduced the surface defects with minimal effect on the heterogeneous substrates. 2) As the seed size increased, the grain size of the film increased. Thus, the density of grain boundaries with a high level of surface trap density was reduced. At the current stage, we did not test $MAPbI_3$ QD seeds for perovkite solar cells, which require for the optimization processes for charge transport layers, photoactive $MAPbI_3$ and metal electrode. However, using the similar approach described in this study, the synthesis of $MAPbI_3$ films using $MAPbI_3$ QD seeds is anticipated to improve solar cell performance due to an reduction of defects in perovskite films.

Finally, the stability of the OHP film under exposure to localized heat generated by an electron beam was evaluated via time-dependent SEM.[48] Figure S8 shows surface images according to the exposure time of the electron beam. The film formed by toluene exhibited cracks on the surface when exposed for 30s. For a film formed with a seed concentration of 4.3%, the cracks appeared at 45s. For a film formed with a seed concentration of 7.0%, there was no cracking for the 45 s. The appearance of the cracks is attributed to the decomposition due to a chain reaction starting from surface defects induced by the electron beam heating. Figure S9a shows an SEM image taken when the film formed by toluene was exposed to the electron beam for approximately 1 min. The atomic percentages of O, C, Br and Pb for the interior and boundary of the crack in the Figure S9a are shown in Figure S9b and Table S2. The atomic percentage of O at the cracked boundary was 38.33, which was higher than that in the interior. The atomic percentages of C, Pb and Br were 31.48, 1.76, and 8.84, respectively, which were lower than those in the interior. The cracks first appeared in the non-stoichiometric grain boundaries, which had a relatively high defect density. The grain boundaries exhibited a high O concentration, which is associated with halogen vacancies.[49] The Pb-Br ratio in the interior was close to the stoichiometric value of 1:3.2, but that at the boundary was 1:5.0, which is close to that for the non-stoichiometric $[PbBr_5]$ complex.[50,51]

Conclusion

In conclusion, we fabricated a [111]-axial directional pyramidal $MAPbBr_3$ thin film crystallized by seeds distributed in toluene. The growth mechanism induced by the seeds was explained by two molecular exchanges according to the solvent of the film solution. By adjusting the seed concentration, the distribution of the (100) and (111) planes was precisely controlled. As the seed size increased, the crystal size of the film increased to 1033 nm. The film crystallized by the seeds exhibited an improved integrated PL intensity (by a factor of approximately 5.3) and improved uniformity compared with the film formed with toluene. Additionally, the surface trap density of the films formed using seeds was 3.5 times lower than that of the films formed using toluene. Furthermore, when the seed were used, the photocurrent was enhanced by a factor of 37, and the photocurrent hysteresis and non-saturated response were suppressed. Moreover, the stability against electron-beam heating was improved via the reduction of surface defects. Thus, the films formed by seeds exhibited improved structural, optical, and electrical properties compared with the films formed without seeds. The special structure of (111)-plane pyramidal $MAPbBr_3$ will contribute significantly to the development of photodetectors as well as solar cells (or tandem solar cell) and light-emitting diodes.

Conflicts of interest

There are no conflicts to declare.

Acknowledgements

This work was supported by IBS-R011-D1 and the National Research Foundation of Korea (NRF) grant funded by the Korea government (MSIP) (2019R1A2B5B02070657). This work was partially supported by the National Science Foundation under projects (1355678 and 1547771), Virginia Microelectronic Consortium program and BCET MRSE grant.

References

1 G. Xing, N. Mathews, S. Sun, S. S. Lim, Y. M. Lam, M. Grätzel, S. Mhaisalkar and T. C. Sum, *Science*, 2013, **342**, 344-347.

 This journal is © The Royal Society of Chemistry 20xx

2 M. Grätzel, *Nature materials*, 2014, **13**, 838.
3 W. S. Yang, B.-W. Park, E. H. Jung, N. J. Jeon, Y. C. Kim, D. U. Lee, S. S. Shin, J. Seo, E. K. Kim and J. H. Noh, *Science*, 2017, **356**, 1376-1379.
4 D. Ghosh, A. R. Smith, A. B. Walker and M. S. Islam, *Chemistry of Materials*, 2018, **30**, 5194-5204.
5 A. Thote, I. Jeon, J.-W. Lee, S. Seo, H.-S. Lin, Y. Yang, H. Daiguji, S. Maruyama and Y. Matsuo, *ACS Applied Energy Materials*, 2019, **2**, 2486-2493.
6 M. Ahmadi, T. Wu and B. Hu, *Advanced Materials*, 2017, **29**, 1605242.
7 C. Xie, P. You, Z. Liu, L. Li and F. Yan, *Light: Science & Applications*, 2017, **6**, e17023.
8 Z. Xu, Z. Liu, Y. Huang, G. Zheng, Q. Chen and H. Zhou, *Journal of Materials Chemistry C*, 2017, **5**, 5810-5817.
9 H. Cho, S.-H. Jeong, M.-H. Park, Y.-H. Kim, C. Wolf, C.-L. Lee, J. H. Heo, A. Sadhanala, N. Myoung and S. Yoo, *Science*, 2015, **350**, 1222-1225.
10 L. Zhang, X. Yang, Q. Jiang, P. Wang, Z. Yin, X. Zhang, H. Tan, Y. M. Yang, M. Wei and B. R. Sutherland, *Nature communications*, 2017, **8**, 15640.
11 W. Hu, W. Huang, S. Yang, X. Wang, Z. Jiang, X. Zhu, H. Zhou, H. Liu, Q. Zhang and X. Zhuang, *Advanced Materials*, 2017, **29**, 1703256.
12 K. Hwang, Y. S. Jung, Y. J. Heo, F. H. Scholes, S. E. Watkins, J. Subbiah, D. J. Jones, D. Y. Kim and D. Vak, *Advanced materials*, 2015, **27**, 1241-1247.
13 N. J. Jeon, J. H. Noh, Y. C. Kim, W. S. Yang, S. Ryu and S. I. Seok, *Nature materials*, 2014, **13**, 897.
14 J. Wu, X. Xu, Y. Zhao, J. Shi, Y. Xu, Y. Luo, D. Li, H. Wu and Q. Meng, *ACS applied materials & interfaces*, 2017, **9**, 26937-26947.
15 S. W. Kang, H. W. Shim, D.-Y. Lee, S.-H. Han, D. J. Kim, J. W. Kim, B. W. Oh, O. Kryliouk and T. J. Anderson, *JOURNAL OF SEMICONDUCTOR TECHNOLOGY AND SCIENCE*, 2006, **6**, 79.
16 R. Aggarwal, H. Zhou, C. Jin, J. Narayan and R. J. Narayan, *Journal of applied physics*, 2010, **107**, 113530.
17 B. J. Foley, J. Girard, B. A. Sorenson, A. Z. Chen, J. S. Niezgoda, M. R. Alpert, A. F. Harper, D.-M. Smilgies, P. Clancy and W. A. Saidi, *Journal of Materials Chemistry A*, 2017, **5**, 113-123.
18 H.-B. Chen, X.-H. Ding, X. Pan, T. Hayat, A. Alsaedi, Y. Ding and S.-Y. Dai, *ACS applied materials & interfaces*, 2018, **10**, 2603-2611.
19 N. Sakai, Z. Wang, V. M. Burlakov, J. Lim, D. McMeekin, S. Pathak and H. J. Snaith, *Small*, 2017, **13**, 1602808.
20 W. S. Yang, J. H. Noh, N. J. Jeon, Y. C. Kim, S. Ryu, J. Seo and S. I. Seok, *Science*, 2015, **348**, 1234-1237.
21 Y. Zhao, H. Tan, H. Yuan, Z. Yang, J. Z. Fan, J. Kim, O. Voznyy, X. Gong, L. N. Quan and C. S. Tan, *Nature communications*, 2018, **9**, 1607.
22 D. Bi, C. Yi, J. Luo, J.-D. Décoppet, F. Zhang, S. M. Zakeeruddin, X. Li, A. Hagfeldt and M. Grätzel, *Nature Energy*, 2016, **1**, 16142.
23 H. Uratani and K. Yamashita, *The journal of physical chemistry letters*, 2017, **8**, 742-746.
24 J.-W. Lee, S.-G. Kim, S.-H. Bae, D.-K. Lee, O. Lin, Y. Yang and N.-G. Park, *Nano letters*, 2017, **17**, 4270-4276.
25 Y. Shao, Z. Xiao, C. Bi, Y. Yuan and J. Huang, *Nature communications*, 2014, **5**, 5784.
26 D. H. Kim, J. Park, Z. Li, M. Yang, J. S. Park, I. J. Park, J. Y. Kim, J. J. Berry, G. Rumbles and K. Zhu, *Advanced Materials*, 2017, **29**, 1606831.
27 N. Cho, F. Li, B. Turedi, L. Sinatra, S. P. Sarmah, M. R. Parida, M. I. Saidaminov, B. Murali, V. M. Burlakov and A. Goriely, *Nature communications*, 2016, **7**, 13407.
28 R. Zhang, W. Cai, T. Bi, N. Zarifi, T. Terpstra, C. Zhang, Z. V. Verdeny, E. Zurek and S. Deemyad, *The journal of physical chemistry letters*, 2017, **8**, 3457-3465.
29 P. Gratia, I. Zimmermann, P. Schouwink, J.-H. Yum, J.-N. Audinot, K. Sivula, T. Wirtz and M. K. Nazeeruddin, *ACS Energy Letters*, 2017, **2**, 2686-2693.
30 X. Du, G. Wu, J. Cheng, H. Dang, K. Ma, Y.-W. Zhang, P.-F. Tan and S. Chen, *RSC Advances*, 2017, **7**, 10391-10396.
31 W. Deng, X. Xu, X. Zhang, Y. Zhang, X. Jin, L. Wang, S. T. Lee and J. Jie, *Advanced Functional Materials*, 2016, **26**, 4797-4802.
32 M. Kumar, A. Kumar and A. Abhyankar, *ACS applied materials & interfaces*, 2015, **7**, 3571-3580.
33 S. Agouram, J. Z. Perez and V. Muñoz-Sanjosé, *Applied Physics A*, 2007, **88**, 83-87.
34 H. F. McMurdie, M. C. Morris, E. H. Evans, B. Paretzkin, W. Wong-Ng and C. R. Hubbard, *Powder Diffraction*, 1986, **1**, 40-43.
35 S. K. Balakrishnan and P. V. Kamat, *ACS Energy Letters*, 2016, **2**, 88-93.
36 W. Nie, H. Tsai, R. Asadpour, J.-C. Blancon, A. J. Neukirch, G. Gupta, J. J. Crochet, M. Chhowalla, S. Tretiak and M. A. Alam, *Science*, 2015, **347**, 522-525.
37 C. Motta, F. El-Mellouhi and S. Sanvito, *Physical Review B*, 2016, **93**, 235412.
38 J.-S. Park, S. Choi, Y. Yan, Y. Yang, J. M. Luther, S.-H. Wei, P. Parilla and K. Zhu, *The journal of physical chemistry letters*, 2015, **6**, 4304-4308.
39 E. M. Hutter, M. C. Gélvez-Rueda, A. Osherov, V. Bulović, F. C. Grozema, S. D. Stranks and T. J. Savenije, *Nature materials*, 2017, **16**, 115.
40 G. Xing, N. Mathews, S. S. Lim, N. Yantara, X. Liu, D. Sabba, M. Grätzel, S. Mhaisalkar and T. C. Sum, *Nature materials*, 2014, **13**, 476.
41 A. Al Mamun, T. T. Ava, K. Zhang, H. Baumgart and G. Namkoong, *Physical Chemistry Chemical Physics*, 2017, **19**, 17960-17966.
42 C.-J. Shih, G. L. Paulus, Q. H. Wang, Z. Jin, D. Blankschtein and M. S. Strano, *Langmuir*, 2012, **28**, 8579-8586.
43 B. Wenger, P. K. Nayak, X. Wen, S. V. Kesava, N. K. Noel and H. J. Snaith, *Nature communications*, 2017, **8**, 590.
44 K. Pandey, M. Chauhan, V. Bhatt, B. Tripathi, P. Yadav and M. Kumar, *RSC Advances*, 2016, **6**, 105076-105080.
45 Y. Rakita, E. Meirzadeh, T. Bendikov, V. Kalchenko, I. Lubomirsky, G. Hodes, D. Ehre and D. Cahen, *APL Materials*, 2016, **4**, 051101.
46 R.-P. Xu, Y.-Q. Li, T.-Y. Jin, Y.-Q. Liu, Q.-Y. Bao, C. O'Carroll and J.-X. Tang, *ACS applied materials & interfaces*, 2018, **10**, 6737-6746.
47 W. Huang, S. J. Yoon and P. Sapkota, *ACS Applied Energy Materials*, 2018, **1**, 2859-2865.
48 C. Xiao, Z. Li, H. Guthrey, J. Moseley, Y. Yang, S. Wozny, H. Moutinho, B. To, J. J. Berry and B. Gorman, *The Journal of Physical Chemistry C*, 2015, **119**, 26904-26911.
49 G. Namkoong, H. J. Jeong, A. Mamun, H. Byun, D. Demuth and M. S. Jeong, *Solar Energy Materials and Solar Cells*, 2016, **155**, 134-140.
50 O. Nazarenko, M. R. Kotyrba, M. Wörle, E. Cuervo-Reyes, S. Yakunin and M. V. Kovalenko, *Inorganic chemistry*, 2017, **56**, 11552-11564.
51 X.-W. Lei, C.-Y. Yue, J.-C. Wei, R.-Q. Li, Y. Li and F.-Q. Mi, *Dalton Transactions*, 2016, **45**, 19389-19398.

Table of contents

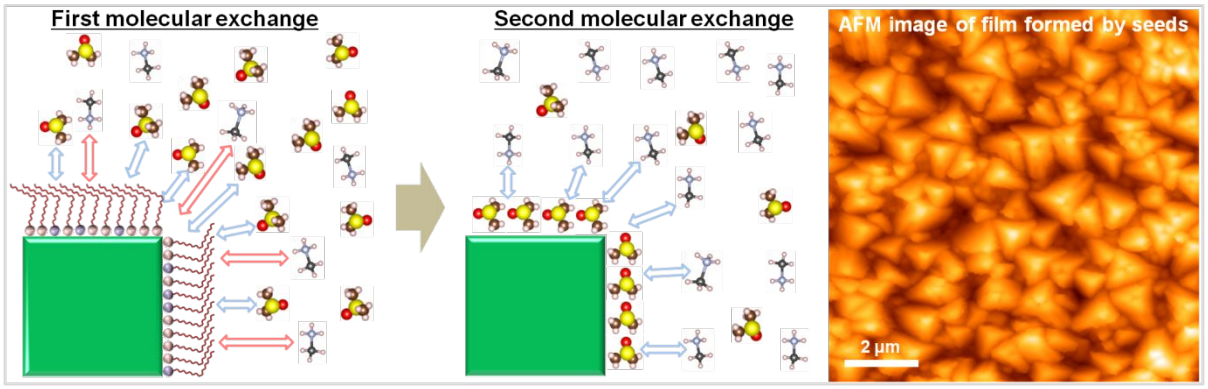

Unique pyramidal $MAPbBr_3$ film is formed by MAPbBr3 seeds. The pyramidal $MAPbBr_3$ film effectively reduces surface defects, eliminating hysteresys from the photodetector.